Open Ceramics 25 (2026) 100916

Contents lists available at ScienceDirect

Open Ceramics

journal homepage: www.sciencedirect.com/journal/open-ceramics

Visible-light-activated Cu and Fe-doped TiO_2 thin films on glass: photocatalytic, antibacterial and self-cleaning performance

Ehsan Mehmandoustesfahani [a], Fatemeh Hakimi [b], Jorge Rodríguez-Chueca [c], José Antonio Díaz–López [a], Antonio Nieto–Márquez [a,*]

[a] Departamento de Ingeniería Mecánica, Química y Diseño Industrial. Escuela Técnica Superior de Ingeniería y Diseño Industrial, Universidad Politécnica de Madrid, Ronda de Valencia 3, 28012 Madrid, Spain
[b] School of Metallurgy and Materials Engineering, College of Engineering, University of Tehran, Tehran, Iran
[c] Departamento de Ingeniería Química Industrial y del Medio Ambiente. Escuela Técnica Superior de Ingenieros Industriales, Universidad Politécnica de Madrid, José Gutiérrez de Abascal 2, 28006 Madrid, Spain

ARTICLE INFO

Keywords:
Metal doped TiO_2
Photocatalysis
Thin films
Hydrophilicity
Escherichia coli

ABSTRACT

In this study, TiO_2 thin films doped with varying loadings of Cu and Fe (0.8, 1.5, 2.2, and 3.0 wt.%) were synthesized via sol–gel dip-coating onto glass substrates at room temperature. The structural and optical properties of the photocatalysts were characterized using X-ray diffraction and specific surface area analyses, field emission scanning electron microscopy (FE-SEM), photoluminescence and UV–Vis spectrophotometry.

Photocatalytic performance was evaluated through methylene blue (MB) degradation, water contact angle (WCA), and *Escherichia coli* inactivation under visible light. Doping TiO_2 with Cu^{2+} and Fe^{3+} affected nanoparticle size and modified optical absorption, reducing the band gap. XRD confirmed anatase as the dominant crystalline phase for both pure and doped TiO_2 calcined at 500 °C, with crystallite sizes of 11–30 nm.

Tauc plot analysis showed band gap narrowing from ~3.20 eV for pure TiO_2 to ~2.65 eV for Fe–TiO_2 and ~2.40 eV for Cu–TiO_2. Cu-doped TiO_2 exhibited enhanced MB degradation at low dopant levels, but activity declined beyond 0.8% Cu, likely due to agglomeration. Fe-doped TiO_2 showed progressive activity increases with higher dopant concentrations. Additionally, 0.8% Cu- and 3% Fe-doped TiO_2 displayed greater hydrophilicity (WCA 9.8° and 18°, respectively) than pure TiO_2 under visible light.

Comparing both dopants, 0.8% Cu-TiO_2 achieved higher MB degradation than 3% Fe–TiO_2. Antibacterial assays revealed that Cu–TiO_2 had superior activity against *Escherichia coli* compared to pure and Fe-doped TiO_2. The best levels for enhanced hydrophilicity and photocatalytic performance were identified as 0.8% Cu and 3.0% Fe, respectively.

1. Introduction

The application of nanotechnology to prevent contamination by toxic chemicals and microbial agents represents one of the most innovative approaches to address challenges in modern healthcare, environmental protection, and smart building systems. Recent research has increasingly focused on materials with photocatalytic properties, particularly for environmental remediation and water purification [1]. The most widely studied semiconductor photocatalysts are ZnO [2], CdS [3], and TiO_2 [4]. Among these, TiO_2 stands out due to its high photocatalytic efficiency, chemical stability, non-toxicity, and cost-effectiveness. It has been extensively utilized in self-cleaning surfaces, volatile organic compound (VOC) removal, as well as in solar cells, sensors, cosmetics, paints, pigments, and antimicrobial coatings [5–7].

The photocatalytic performance of TiO_2 strongly depends on its particle size, crystallinity, and morphology [8]. However, its relatively wide band gap (~3.2 eV) [9] restricts its activation to the ultraviolet region, limiting its efficiency under visible light irradiation [10]. To overcome this limitation, significant efforts have been devoted to extending the light absorption range of TiO_2. One widely explored strategy is metal ion doping, which can reduce the band gap and inhibit the recombination of photogenerated electron–hole pairs. Nevertheless, it has also been observed that excessive dopant concentrations may

* Corresponding author.
E-mail address: antonio.nieto@upm.es (A. Nieto–Márquez).

https://doi.org/10.1016/j.oceram.2026.100916
Received 18 December 2025; Received in revised form 21 January 2026; Accepted 25 January 2026
Available online 26 January 2026

enhance recombination rates. Therefore, determining the optimal dopant concentration is crucial to maximize visible-light photocatalytic efficiency while minimizing charge carrier recombination.

Doping TiO_2 with transition metal ions such as Cu [11] and Fe [12] has emerged as an effective method to reduce band gap energy and improve photocatalytic activity under visible light. Enhancing photocatalytic efficiency primarily relies on two factors: narrowing the band gap and suppressing electron–hole recombination.

The photocatalytic performance of TiO_2 thin films on glass has been investigated since the 1990s as a scalable and recoverable alternative to powder forms. In this sense, sol-gel coatings were first shown to degrade pollutants efficiently in the works of Negishi [13] and Nam [14]. Subsequent studies in the 2000s, including those by Bahnemann and co-workers [15], explored correlations between film structure, preparation procedure and photocatalytic activity. These earlier investigations established the feasibility of immobilizing TiO_2 on glass, but they also revealed intrinsic challenges such as limited catalyst loading and reduced surface area compared to powders. Building on this foundation, more recent research has shifted towards strategies that integrate dopants, novel supports, and hybrid materials to enhance performance while addressing practical issues of scalability and catalyst recovery. For instance, Pava-Gómez et al. [16] synthesized copper-doped TiO_2 catalysts onto glass and low-density polyethylene supports, achieving 68.1–72.8 % methylene blue (MB) degradation in 6 h. Mokhtari et al. [17] developed Ag/TiO_2 photocatalysts thin films onto glass substrates for the photodegradation of diphenhydramine and venlafaxine under UV–Vis irradiation, achieving 70 % of drug removal.

In this work, we report the preparation of Cu- and Fe-doped TiO_2 thin films supported on glass, which not only exhibit photocatalytic activity but also demonstrate significant antibacterial performance and superhydrophilicity under visible light, a feature scarcely explored in earlier studies. Also, this work compares the effects of these dopants on photocatalytic activity in both applications and discusses their mechanisms in dye removal and *Escherichia coli* inactivation under visible light.

2. Experimental

2.1. Chemicals

All chemicals used were analytical grade and were used as received without further purification. Titanium tetraisopropoxide (TTIP) with a purity of 97 wt. % (Aldrich) was used as the titanium precursor, and hydrochloric acid (HCl, 37 wt. %, Merck) was used as the peptization agent. Methylene Blue, Isopropanol (99 wt. %), copper nitrate trihydrate ($Cu(NO_3)_2{\cdot}3H_2O \geq$ 98.0 wt. %), iron nitrate nonahydrate ($Fe(NO_3)_2{\cdot}9H_2O \geq$ 98.0 wt. %), and isopropanol ($\geq$ 99.5 wt. %) were purchased from Sigma–Aldrich.

2.2. Preparation method

Synthesis of TiO_2 sols was carried out using the sol–gel method under continuous stirring. A pure TiO_2 sol was prepared by adding 8 mL of TTIP dropwise into a mixture solution of 80 mL isopropanol and 5 mL HCl 37 wt. %. In turn, Cu and Fe doped sols were prepared by dissolving $Cu(NO_3)_2{\cdot}3H_2O$ and $Fe(NO_3)_2{\cdot}9H_2O$ in a mixed solution of 80 mL isopropanol and 5 mL HCl, based on the desired Cu and Fe content (0.8, 1.5, 2.2 and 3.0 wt percentage of dopant to the total TiO_2 + dopant), followed by the addition of 8 mL TTIP dropwise. The mixture was further stirred for 4 h. For simplicity, xCu– and xFe–doped TiO_2 (x = 0.8, 1.5, 2.2 and 3.0) is adopted as photocatalyst nomenclature. The prepared sols were deposited on ultra–clean glass substrates (5 × 5 cm) using the dip coating process at room temperature with a drowning speed of 4 mm/s. Initial samples were prepared by drying pure TiO_2, Cu and Fe doped TiO_2 films at room temperature for 24 h, followed by drying at 150 °C in an oven. The films were then calcined in a muffle furnace at 500 °C for 2 h to obtain crystalline Cu and Fe–doped TiO_2 thin films. This synthesis procedure is illustrated in Fig. 1.

2.3. Characterization

The crystallographic phases of the synthesized nanoparticles were identified using a Siemens Krystalloflex D5000 unit using a graphite monochromator with Cu Kα (1,2). The samples were scanned over the range $20^\circ \leq 2\theta \leq 80^\circ$. The surface morphology and particle size of thin films were determined by FESEM (JSM–7001FLV, JEOL, Tokyo, Japan), equipped with an INCAx–Sight EDX detector (Oxford Instruments). Optical properties were investigated using UV–Vis diffuse reflectance spectroscopy (DRS) within the 200–800 nm range through UV–Vis spectrophotometer (Lambda 650, Perkin Elmer, Massachusetts, USA). Photoluminescence (PL) emission spectra of the prepared samples were measured using a Cary Eclipse fluorescence spectrophotometer (Varian, Inc., USA) at room temperature, with an excitation wavelength of 320 nm for Fe doped TiO_2 and 410 nm for Cu doped TiO_2. Pure TiO_2 was measured at both excitation wavelengths. A Jikan – Cag 20 SE instrument equipped with high resolution digital camera was used to measure the water contact angle (WCA) on prepared pure and doped TiO_2 thin films. The specific surface area (SSA) was measured using a V–Sorb 2800S surface area analyzer (China) with N_2 as the sorbate at 77 K. All samples were outgassed prior to analysis under vacuum. Total specific surface areas were determined by the Brunauer-Emmett-Teller (BET) analysis.

2.4. Photoactivity measurements

The photocatalytic activity of the coated glass samples was assessed through the degradation of methylene blue (MB) under visible light irradiation. In a typical experiment, 30 mL of a 10 ppm MB aqueous solution was placed in contact with the prepared photocatalyst samples within a custom-made setup consisting of a sealed glass dish. The system was irradiated using a 100 W LED lamp (8000 lm), housed in a light-condensing fixture, for a duration of 5 hours.

Prior to light exposure, the reaction mixture was stirred in the dark for 30 min to establish adsorption–desorption equilibrium between MB molecules and the photocatalyst surface. During irradiation, the solution was continuously stirred using a magnetic stirrer to ensure homogeneity.

Aliquots were withdrawn at regular time intervals to monitor the photocatalytic degradation process. The residual MB concentration in the solution was determined using a UV–Vis spectrophotometer, as described in the previous section. The characteristic absorption peak of MB at approximately 664 nm (λ_{max}) was used to quantify the remaining dye concentration throughout the reaction.

2.5. Antibacterial properties

The antibacterial activity of the bare glass substrate, pure TiO_2 thin films, and doped TiO_2 thin films against *Escherichia coli* strains was evaluated using the plate-counting method in accordance with the JIS Z2801 standard. *Escherichia coli* (ATCC–25922) was purchased from LGC Standards. Prior to testing, all thin film samples and Petri dishes were sterilized in an autoclave at 120 °C for 40 minutes.

Bacterial cultures were incubated at 37 °C for 24 hours, after which they were diluted in deionized (DI) water to achieve an initial concentration of 10^4 colony-forming units per millilitre ($CFU{\cdot}mL^{-1}$). A 10 μL aliquot of the bacterial suspension was deposited onto the surface of each sample. The samples were then irradiated with visible light using a 150 W halogen lamp (OSRAM Co.) for exposure times of 60, 120, and 180 minutes.

Following irradiation, the surfaces were rinsed with 900 μL of sterilized phosphate-buffered saline (PBS). From this solution, 100 μL aliquots were plated onto nutrient agar and incubated at 37 °C for 24 hours. The number of bacterial colonies was counted to determine the

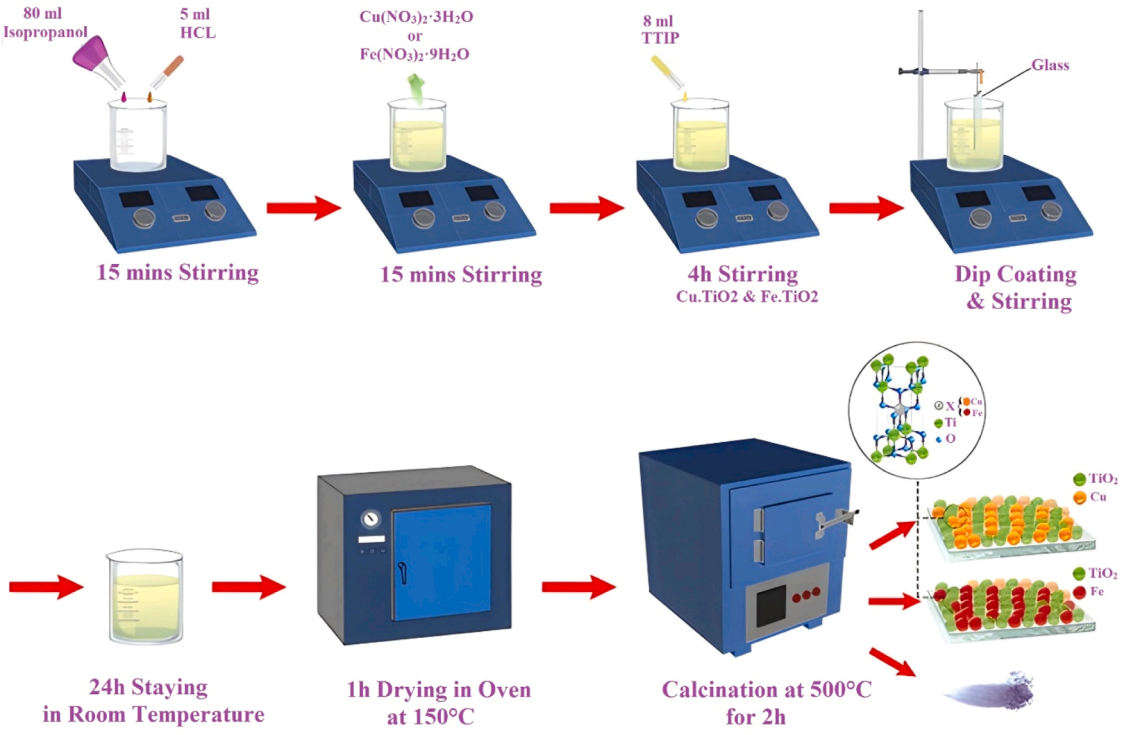

Fig. 1. Schematic procedure for the synthesis of Cu–TiO_2 and Fe–TiO_2 samples.

antibacterial efficiency.

3. Results and discussion

3.1. X–ray diffraction (XRD) and specific surface area results

X-ray diffraction (XRD) analysis was carried out to investigate the phase composition and crystalline structure of pure TiO_2, xCu–TiO_2 and xFe–TiO_2 nanoparticles at various doping levels (0.8, 1.5, 2.2, and 3.0 wt. %). Fig. 2 displays the characteristic diffraction peaks of the anatase phase at 2θ values of 25.40°, 37.04°, 37.84°, 38.67°, 48.14°, 54.40°, 55.17°, 62.79°, 69.00°, 70.38°, 75.12°, and 76.17°, corresponding to the (101), (103), (004), (112), (200), (105), (211), (204), (116), (220), (215), and (031) crystallographic planes, respectively [18].

In addition, three diffraction peaks are observed at 35.8°, 38.67°, and 48.8° in Cu doped samples with copper content larger than 0.8 wt. % which are attributed to CuO, indicating the formation of a secondary CuO phase. These peaks are indexed to the (002), (111), and (110) planes of monoclinic CuO, respectively (JCPDS card no. 89–2531).

All undoped, Fe–TiO_2, and Cu–TiO_2-doped samples exhibit an anatase crystalline structure, as evidenced by the XRD patterns shown in Fig. 2. The pure anatase TiO_2 phase (space group $I4_1/amd$, JCPDS card no. 21–1272) was used as a reference to identify the phases present. Although dopant ions were incorporated, no significant alteration of the tetragonal structure of TiO_2 was observed. Distinct diffraction peaks corresponding to Fe or Cu were not detected, with the exception of those attributed to CuO, as previously discussed. However, incorporation of dopants induces lattice strain within the anatase structure, resulting in changes in crystallite size and associated dislocation density.

The crystallite sizes of pure and doped TiO_2 samples were calculated using the Debye–Scherrer equation (Eq. (1)):

$$D = \frac{0.9\lambda}{\beta COS\theta} \tag{1}$$

where D is the crystallite size, λ is the X-ray wavelength, β is the full width at half maximum (FWHM) of the peak, θ is the Bragg angle, and 0.9 is the shape factor [8].

Table 1 summarizes the average crystallite size, dislocation density, band gap energy and specific surface area for all samples. The smallest crystallite sizes values are related to 0.8 wt. % Cu and 3.0 wt. % Fe doped samples, which are 11.98 nm and 18.90 nm respectively.

A clear correlation is observed between crystallite size, dislocation density and surface area. As crystallite size decreases, both surface area and dislocation density increase [19]. Dislocation density was derived from crystallite size according to the Eq. (2):

$$\delta = \frac{1}{D^2} \tag{2}$$

Where D is the crystallite size.

Crystallite size results can be ascribed to the smaller ionic radius of Cu^{2+} (0.57 Å) and Fe^{3+} (0.64 Å) in comparison to Ti^{4+} (0.68 Å), which may lead to a reduction in crystallite size when dopant ions are introduced into the TiO_2 matrix. In the case of Fe doping, more stress and dislocation density at higher doping levels can account for a smaller crystallite size, with associated larger SSA. However, the presence of CuO clusters for Cu doping levels higher than 0.8 wt. % can explain the reverse trend followed by these samples, where larger agglomerations are usually accompanied by lower crystal defects such as dislocation density. This trend leads to a decrease in SSA from 58.2 to 30.4 $m^2\ g^{-1}$, while the crystallite size increases from 11.98 to 27.55 nm [19–24].

3.2. Field emission scanning electron microscopy (FESEM) and energy dispersive spectroscopy (EDS) results

The surface morphology and elemental composition of the synthesized samples were characterized using field-emission scanning electron microscopy (FE-SEM) and energy-dispersive X-ray spectroscopy (EDS).

As depicted in Fig. 3, FE-SEM images of undoped TiO_2 and TiO_2 doped with varying concentrations of Cu and Fe reveal significant differences in particle size and morphology. The sample containing 0.8 wt. % Cu displays the smallest particle size, approximately 28 nm, with a uniform spherical morphology, as determined using *ImageJ* software

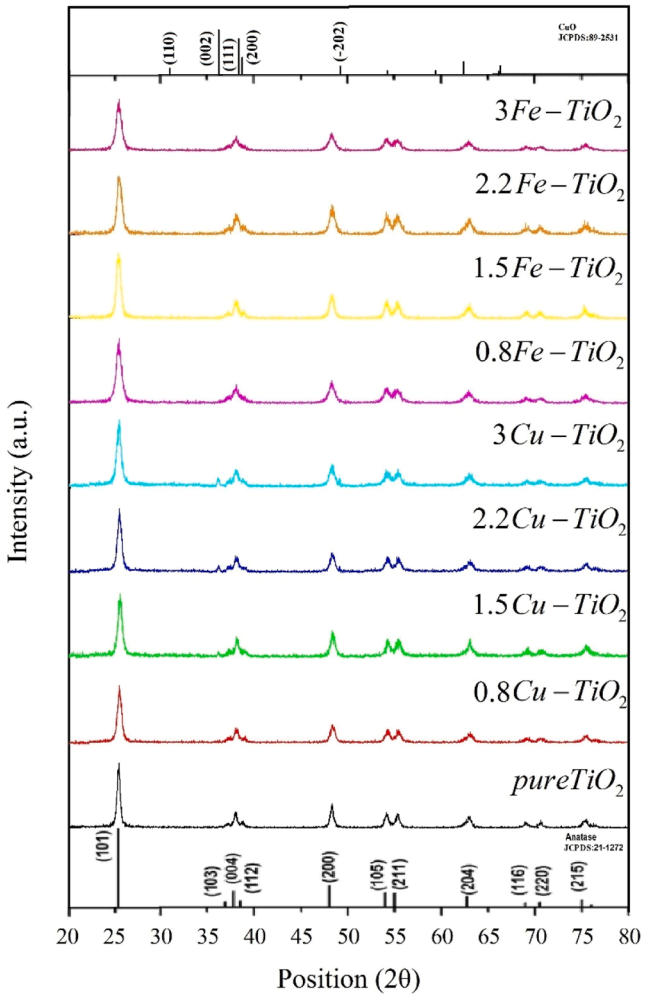

Fig. 2. XRD patterns of pure TiO_2, Cu–TiO_2 and Fe–TiO_2 samples.

Table 1
Structural properties of thin films of TiO_2 and TiO_2 doped with Cu and Fe.

Sample	$D \times 10^{-9}$ m	$\delta \times 10^{14}$ lines/m^2	Band Gap (eV)	SSA/m^2 g^{-1}
Undoped TiO_2	37.45	7.13	3.20	2.0
0.8Cu–TiO_2	11.98	69.67	2.40	58.2
1.5Cu–TiO_2	17.72	31.84	2.70	43.6
2.2Cu–TiO_2	22.42	19.89	2.78	37.5
3Cu–TiO_2	27.55	13.17	3.00	30.4
0.8Fe–TiO_2	30.28	10.90	3.18	27.9
1.5Fe–TiO_2	26.56	14.17	3.00	33.3
2.2Fe–TiO_2	23.50	18.10	2.82	34.9
3Fe–TiO_2	18.90	27.99	2.65	45.2

(Fig. 3a). As the Cu dopant concentration increases from 1.5 to 3 wt. % (Fig. 3b–d), a noticeable agglomeration of nanoparticles is observed, resulting in an increment in average particle size. In contrast, Fe doping induces a reduction in particle size with increasing dopant content (Fig. 3e–h), and no agglomeration is observed across the studied concentrations. 3Fe–TiO_2 sample exhibits the smallest particle size within the Fe series, with an average diameter of approximately 75 nm, and maintains a spherical morphology. For comparison, pure TiO_2 nanoparticles (Fig. 3i) are also nearly spherical but exhibit a significantly larger mean particle size of ~120 nm.

These observations suggest that Cu doping tends to promote nanoparticle coalescence at higher loadings, while Fe doping enhances particle dispersion and size control, which may have important implications for the surface properties and functional performance of the materials. These results are consistent with the trend in crystallite size obtained by XRD.

Energy-dispersive X-ray spectroscopy (EDS) was employed to determine the elemental composition of all synthesized samples. Table 2 shows the EDS outputs of pure TiO_2, Cu–TiO_2, and Fe–TiO_2 nanoparticles at various doping levels (0.8, 1.5, 2.2, and 3.0 wt. %). Obtained results confirm the presence of Ti, O, Cu, and Fe in the corresponding samples, with measured dopant concentrations closely matching the theoretical values. For this reason, and for the sake of simplicity, theoretical values will be used throughout the text to identify the photocatalysts.

3.3. UV–Vis absorption and bandgap estimation

Fig. 4 shows the UV–Vis absorption spectra and the corresponding Tauc plots for pure TiO_2, Cu- and Fe-doped TiO_2 thin films at varying dopant weight percentages. These analyses highlight the influence of doping on the optical properties and band gap of TiO_2.

As illustrated in Fig. 4a, 0.8Cu–TiO_2 sample exhibits the most pronounced red shift in the absorption edge, extending the absorption range into the visible region (320–440 nm). Furthermore, the area under the absorbance–wavelength curves increases upon doping, indicating enhanced visible-light absorption by the doped samples.

The optical band gap energy (Eg) of both undoped and doped TiO_2 samples was estimated using the Kubelka–Munk function, with Tauc plots generated by plotting $A = [F(R)\cdot h\nu]^{1/2}$ *vs* photon energy ($h\nu$), as shown in Fig. 4(a′, b′, c′) [25,26]. According to these plots, the undoped TiO_2 sample exhibits a band gap of 3.20 eV, while the 0.8Cu– TiO_2 sample displays the lowest band gap at 2.40 eV.

Interestingly, Cu concentrations above 0.8 wt. % result in wider band gaps compared to the 0.8Cu– TiO_2 sample. This phenomenon suggests that excessive Cu doping, associated with CuO formation, introduces structural disorder that reduces free carrier density, causing Cu atoms to act as trap centres rather than electron donors [27]. The apparent widening of the band gap at higher dopant concentrations can be attributed to the Burstein–Moss effect [28,29]. In this context, increased donor electron concentration from Cu leads to the filling of conduction band states. As a result, higher photon energies are required to excite electrons from the valence band to the unoccupied states in the conduction band, effectively increasing the observed band gap. This is accompanied by an upward shift in the Fermi level and a blue shift in the absorption edge for heavily doped samples relative to those with lower Cu content [30,31]. It is worth noting that Cu– TiO_2 samples with 1.5, 2.2, and 3.0 wt percentages remains at longer wavelengths (and lower band gaps) than that of pure TiO_2.

The trend observed for Cu doping was not replicated in the case of Fe doping. As shown in Fig. 4b, the 3Fe– TiO_2 sample exhibits the most pronounced red shift in the absorption edge compared to samples with lower Fe doping levels (0.8, 1.5, and 2.2 wt. %) and pure TiO_2. This indicates that at a dopant concentration up to 3 wt. %, Fe incorporation effectively narrows the band gap without inducing significant agglomeration or structural disorder at this level. Fig. 4(b′) presents the calculated band gap energies for Fe–TiO_2 samples at different Fe doping concentrations. The lowest band gap value, 2.65 eV, corresponds to the 3Fe–TiO_2 sample, confirming the enhanced visible-light absorption capability at this doping level.

The mechanism behind the band gap reduction upon doping with transition metals is associated with the formation of sub-bands near the conduction band due to the presence of Cu^{2+} and Fe^{3+} ions. These sub-bands result from *sp–d* exchange interactions between conduction band electrons and the localized *d*-electrons of Cu^{2+} and Fe^{3+} ions that substitute Ti^{4+} sites in the TiO_2 lattice.

These *s–d* and *p–d* interactions cause a downward shift of the conduction band edge and an upward shift of the valence band edge, leading to a narrowed band gap. The incorporation of these metal ions lowers the conduction band energy, which accounts for the reduced band gap

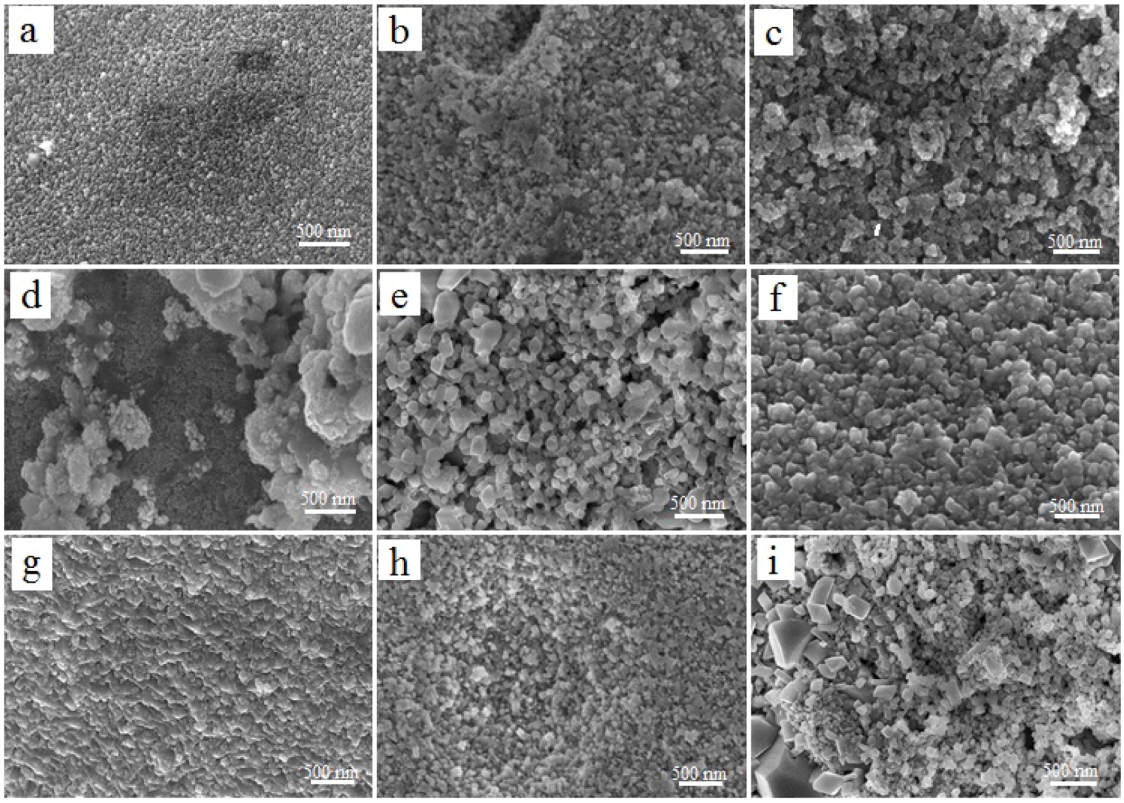

Fig. 3. FE-SEM micrographs of (a-d) Cu–TiO_2 (xCu–TiO_2) (e-h) Fe–TiO_2 (xFe–TiO_2), (i) pure TiO_2, where x represents the doping content for 0.8, 1.5, 2.2, and 3.0 wt. %, respectively.

Table 2
EDS results of (a) pure TiO_2, xCu–TiO_2 and xFe–TiO_2, where x represents the theoretical doping wt. % for 0.8, 1.5, 2.2, and 3.0, respectively.

Sample	Element	Wt %	Sample	Element	Wt %
Pure TiO_2	Ti	37.17			
	O	62.85			
	Ti	35.18		Ti	35.14
0.8Cu–TiO_2	O	64.13	0.8Fe–TiO_2	O	64.17
	Cu	0.69		Fe	0.69
	Ti	30.85		Ti	45.27
1.5Cu–TiO_2	O	67.75	1.5Fe–TiO_2	O	53.35
	Cu	1.40		Fe	1.38
	Ti	42.17		Ti	31.08
2.2Cu–TiO_2	O	55.91	2.2Fe–TiO_2	O	66.89
	Cu	1.92		Fe	2.03
	Ti	34.27		Ti	34.15
3Cu–TiO_2	O	63.14	3Fe–TiO_2	O	63.03
	Cu	2.59		Fe	2.82

observed in Cu- and Fe-doped TiO_2 nanocrystals [10,32].

The narrowed band gap and broadening of the absorption edge into the visible region enhance light harvesting, while the formation of sub-bands increases the electron–hole recombination time, thereby improving photocatalytic performance. Therefore, doping TiO_2 with Cu^{2+} or Fe^{3+} ions has proven to be an effective strategy to improve its optical response under visible light compared to undoped TiO_2. The best doping conditions within the range evaluated, in terms of band gap reduction, are achieved at 0.8 Cu and 3.0 Fe weight percentages, corresponding to band gaps of 2.40 eV and 2.65 eV, respectively, as shown in Fig. 4(c).

3.4. Photoluminescence evaluations

Photoluminescence (PL) spectroscopy was employed to evaluate the photoinduced electron–hole recombination behavior of pure TiO_2 and Cu- and Fe-doped TiO_2 samples (Fig. 5) [33,34]. The PL intensity of a semiconductor is directly related to the recombination rate of photo-generated electron–hole pairs; therefore, higher PL intensity indicates faster recombination and, consequently, lower photocatalytic efficiency [35].

The major peak at around 400 nm has been previously associated in the literature with recombination transitions from the conduction band to the valence band of TiO_2 [36], as well as band gap, defects, or surface trapping of electrons [37]. The intensity of this peak consistently decreased for doped samples, indicating a slower recombination in these photocatalysts. This intensity was higher for larger Cu loadings in Cu-doped samples, as shown in Fig. 5a, and consistent with the reported in [37]. However, for the Fe-doped samples (Fig. 5b), this trend was reverse, in line with results shown above regarding particle size, band gap and specific surface area. It is also worth flagging the peaks appearing in the range 475–530 nm, in pure and Cu-doped samples, associated to a self-trapping of electrons by the TiO_6 octahedra. This result strengthens the idea of the different impact of Fe and Cu incorporation in the anatase microstructure. These differences highlight how each dopant uniquely affects the photoluminescent properties of titanium dioxide, and in line, its photocatalytic activity [38].

3.5. Photocatalytic degradation of MB

The photocatalytic activity was assessed by monitoring the removal of MB in aqueous solution under visible LED lamp irradiation. Fig. 6 illustrates the photocatalytic performance of Cu–TiO_2 and Fe–TiO_2 samples doped with varying concentrations of Cu and Fe, respectively, in comparison with bare glass and undoped TiO_2 for the degradation of

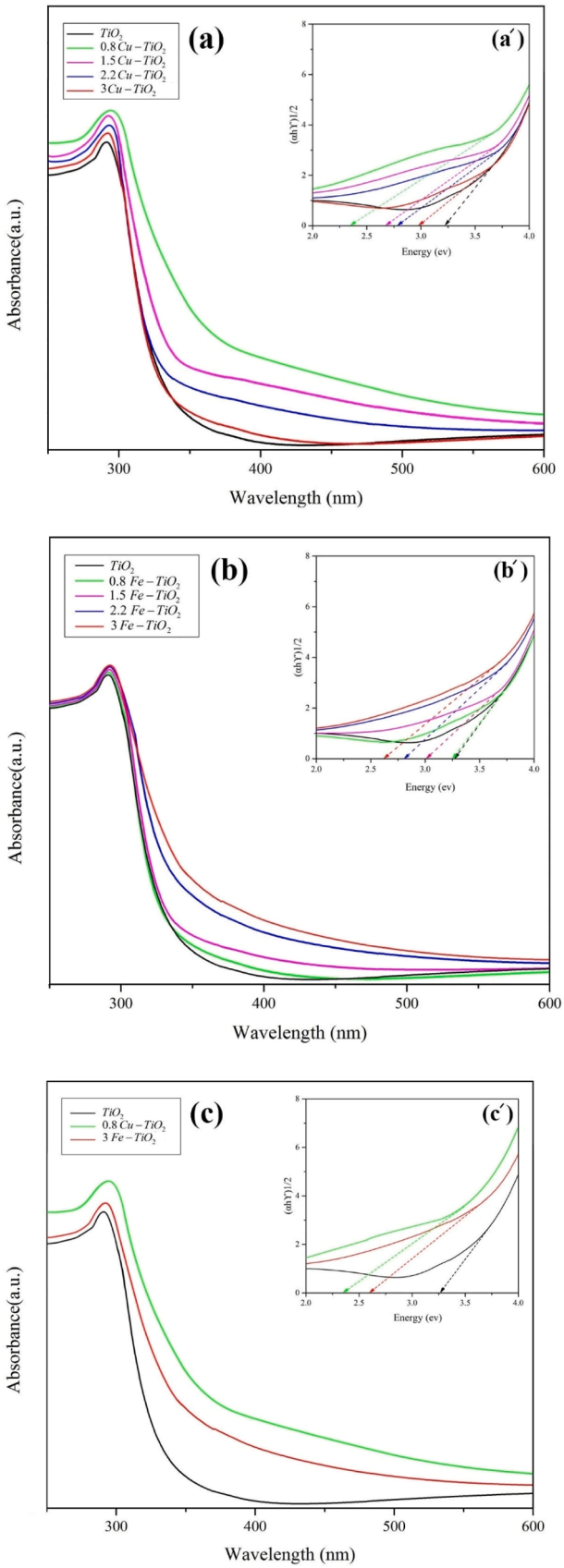

Fig. 4. UV–Vis absorption spectra of (a) xCu–TiO_2, (b) xFe–TiO_2 (x = 0.8, 1.5, 2.2, 3), (c) TiO_2, 3Fe–TiO_2 and 0.8Cu–TiO_2 samples. Inset: (a) Eg of x Cu– TiO_2, (b) Eg of xFe–TiO_2, (c) Eg of TiO_2, 3Fe–TiO_2 and 0.8Cu–TiO_2 samples.

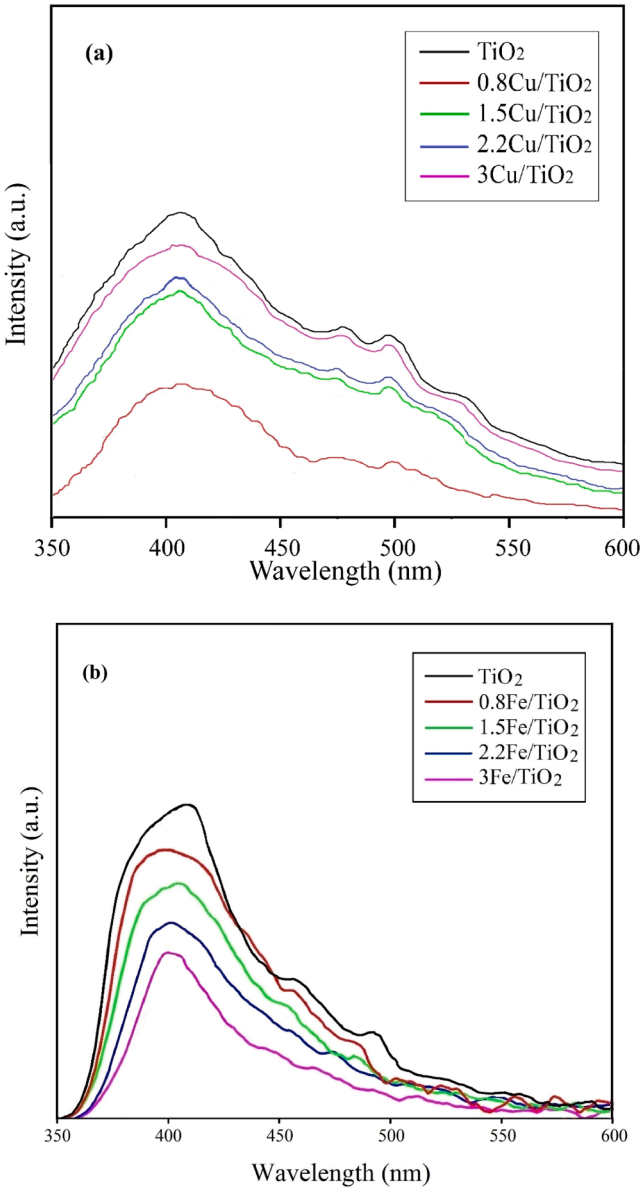

Fig. 5. PL spectra of (a) xCu–TiO_2, (b) xFe–TiO_2 (x = 0.8, 1.5, 2.2, and 3).

10 ppm MB.

As shown in Fig. 6a, the 0.8Cu–TiO_2 sample exhibited the highest removal efficiency, achieving approximately 80 % removal after 300 min. In Fig. 6b, a positive correlation is observed between Fe content and MB removal, with the 3Fe–TiO_2 sample reaching a maximum removal of around 65 %.

Several factors contribute to the enhanced photocatalytic activity observed in the Cu– and Fe–doped TiO_2 samples. Firstly, as evident in Figs. 4a and 4b, the absorbance spectra of the doped samples show increased light absorption in the visible region, enabling more efficient light harvesting for photocatalysis [39]. Secondly, the doped samples exhibit narrower band gaps compared to pure TiO_2 (Figs. 4(a′) and 4 (b′)), facilitating electron transfer from the TiO_2 valence band to the conduction bands associated with Cu^{2+} and Fe^{3+} ions. This process promotes the formation of a Schottky barrier at the metal–semiconductor interface, enhancing charge carrier separation and thereby improving photocatalytic performance [40]. Additionally, the impurity energy levels introduced by Cu and Fe doping extend the lifetime and separation of photo-induced electron–hole pairs, as demonstrated by PL measurements. Previous studies suggest that Cu and Fe incorporation

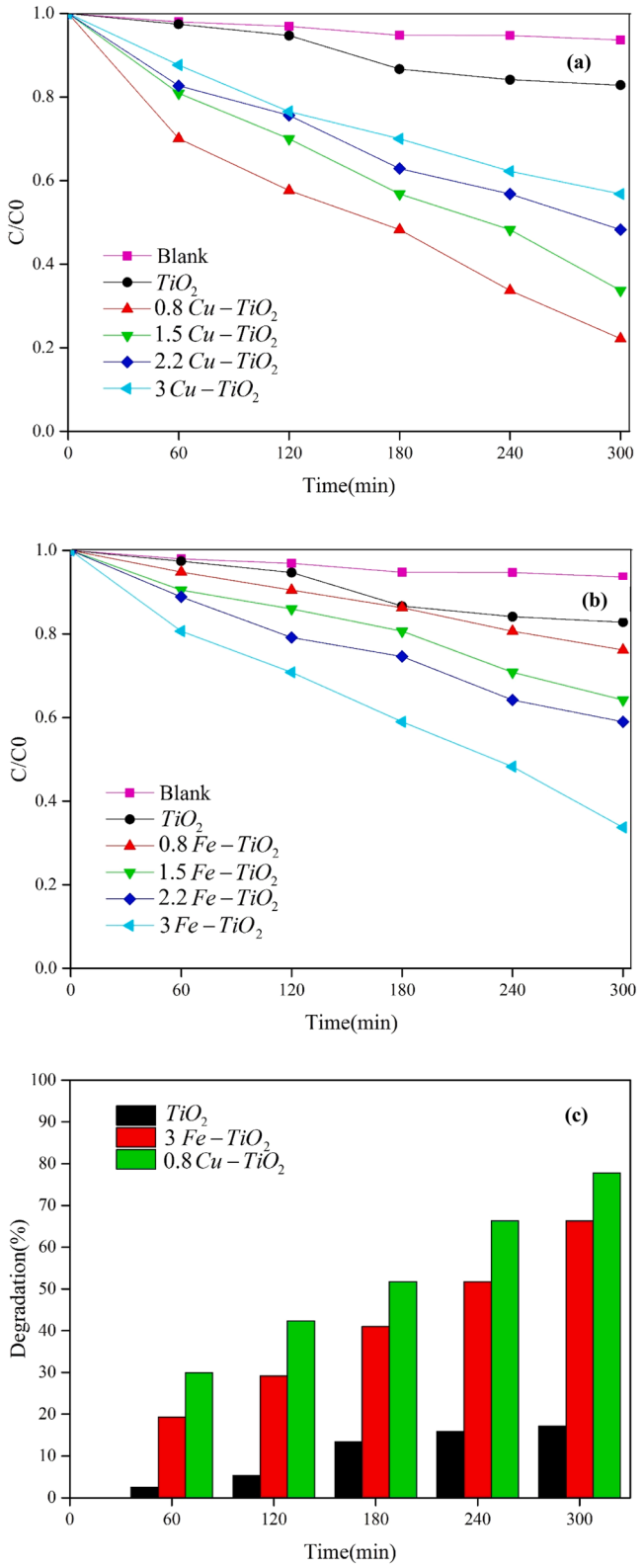

Fig. 6. MB concentration ratio (C/Co) as a function of time for (a) xCu–TiO_2 and (b) xFe–TiO_2 (x = 0.8, 1.5, 2.2 and 3). (c) Comparison, in terms of degradation percentage of MB, of best doped catalyst with pure TiO_2. Blank stands for experiments with the bare glass support.

generates oxygen vacancies that act as active sites for water dissociation on the TiO_2 surface, suppressing electron–hole recombination and further enhancing photocatalytic activity [41,21]. The superior performance of the 0.8Cu–TiO_2 sample is attributed not only to its enhanced optical properties but also to the crystalline phases identified in the XRD analysis (Fig. 2). In this sample, Cu^{2+} ions act as electron acceptors from the TiO_2 conduction band, facilitating the reduction of oxygen molecules to superoxide anions ($^{\bullet}O_2^-$). These anions complement the roles of holes (h^+) and hydroxyl radicals ($^{\bullet}OH$) in the photocatalytic process. Thus, surface modification of TiO_2 with a lower Cu concentration (0.8 wt. %) enhances charge carrier separation and photocatalytic activity through metal-to-metal charge transfer via Ti–O–Cu complexes. Here, Cu^{2+} primarily functions as an electron trap, reducing recombination rates and boosting photocatalytic efficiency [42]. However, Cu doping levels above 0.8 wt. % lead to the formation of isolated CuO clusters, as indicated by XRD results. These aggregates may act as charge recombination centres, hindering mass transport and reducing the available surface area by partially blocking TiO_2 active sites, ultimately decreasing light absorption and photocatalytic performance. Therefore, while Ti–O–Cu bonds enhance photocatalytic activity, Cu–O–Cu bonds formed in CuO nanoclusters may have a detrimental effect. Moreover, the 0.8Cu–TiO_2 sample exhibits the smallest particle size and the largest surface area, further contributing to its superior photocatalytic efficiency [42].

A comparison of 0.8Cu–TiO_2, 3Fe–TiO_2, and pure TiO_2 is presented in Fig. 6(c). The 0.8Cu–TiO_2 sample demonstrated the highest photocatalytic performance, achieving 80 % degradation under visible-light irradiation after 300 min, compared to 65 % for 3Fe–TiO_2 and only 15 % for undoped TiO_2.

MB removal as a function of reaction time was fitted to a first order model, as shown in Fig. 7, according to Eq. (3):

$$-Ln\left(\frac{C_0}{C}\right) = kt \tag{3}$$

Where k, t (min), C_o (mg/L), and C (mg/L) represent the first-order rate constant, removal time, initial dye concentration, and concentration at time t, respectively. The results indicate that the removal of MB follows a first-order kinetic model. The rate constants for MB removal using 0.8Cu– TiO_2, 3Fe– TiO_2, and pure TiO_2 were found to be 0.0047, 0.0032, and 0.0007 min^{-1}, respectively, as shown in Table 3. As expected, the 0.8Cu– TiO_2 sample exhibited the highest rate constant, reflecting superior photocatalytic performance compared to the other materials [43,44]. These values, although lower than those reported by other studies using powdered photocatalysts (e.g., 0.0120 min^{-1} for 0.1Cu– TiO_2 and 0.0088 min^{-1} for 0.1Fe– TiO_2) [45], are still in close agreement. The slightly reduced k values observed in this study can be attributed to the immobilization of the active phase as a thin film on a glass substrate, which inherently limits the available surface area and active sites compared to suspended powders. Indeed, the k value of 0.8Cu/TiO_2 obtained in this work was higher than that reported by Pava-Gómez et al. (0.0024 min^{-1}) [16], who synthesized Cu/TiO_2 photocatalyst thin films onto glass substrate.

3.5. Mechanism of photocatalytic removal of MB

To understand the origin of the enhanced photocatalytic activity, it is essential to discuss the underlying charge transfer processes. When TiO_2 is irradiated with light of energy greater than its band gap, electron–hole pairs are generated. Specifically, the photogenerated electrons can react with O_2 molecules to form superoxide radicals ($^{\bullet}O_2^-$), while the holes can oxidize OH^- or H_2O to produce hydroxyl radicals ($^{\bullet}OH$). These reactive oxygen species, along with other oxidizing agents, are primarily responsible for the photoremoval of MB [46].

The overall photocatalytic mechanism on TiO_2 has been described above; however, the addition of dopants such as Fe^{3+} and Cu^{2+}

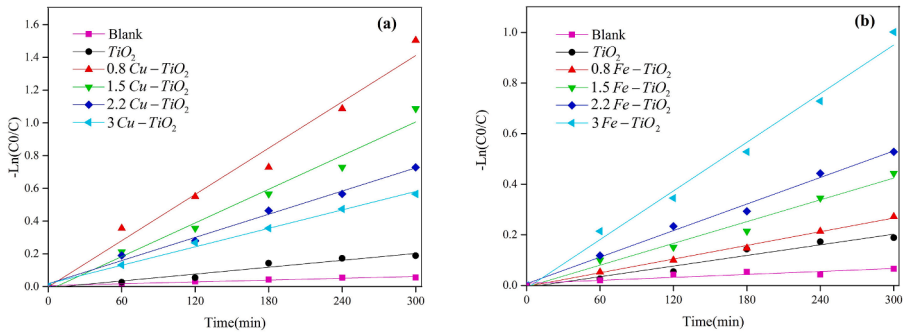

Fig. 7. Plots of –ln(C_0/C) vs irradiation time (min) for photocatalytic removal of MB (a) xCu–TiO_2 and (b) xFe–TiO_2 (x = 0.8, 1.5, 2.2 and 3.0), respectively.

Table 3
First-order rate constants (k) and linear regression coefficients for MB.

Photocatalyst	k (min^{-1})	R^2
TiO_2	0.0007	0.95988
0.8Cu–TiO_2	0.0047	0.97366
1.5Cu–TiO_2	0.0034	0.97532
2.2Cu–TiO_2	0.0023	0.99107
3Cu–TiO_2	0.0018	0.99343
0.8Fe–TiO_2	0.0009	0.99534
1.5Fe–TiO_2	0.0014	0.97671
2.2Fe–TiO_2	0.0017	0.99055
3Fe–TiO_2	0.0032	0.98672

significantly enhances the photocatalytic performance. A schematic illustration of the visible light–driven photocatalytic reactions along with a comparison of their effects occurring on the surface of Fe and Cu doped TiO_2, is presented in Fig. 8.

The enhancement in the photocatalytic activity of TiO_2 through Fe^{3+} and Cu^{2+} ion doping can be primarily attributed to the suppression of photogenerated electron–hole recombination. Additionally, doping introduces Cu and Fe *d*-orbitals within the band gap of TiO_2, thereby reducing the band gap energy from 3.20 eV to 2.65 eV and 2.40 eV for 3Fe–TiO_2 and 0.8Cu– TiO_2, respectively, as reported above. This band gap narrowing facilitates the generation of more electron (e^-) and hole (h^+) pairs under visible light irradiation compared to pure TiO_2, thus significantly enhancing the photocatalytic performance of the doped samples. These *d* orbitals give rise to two types of energy levels, as indicated in Fig. 8. the oxidation levels Fe^{3+}/Fe^{4+} for Fe and Cu^{+}/Cu^{2+} for Cu are located above the valence band, while the reduction levels Fe^{3+}/Fe^{2+} and Cu^{2+}/Cu^{+} are located below the conduction band of pure TiO_2. The mechanism of Fe–TiO_2 is described by the Eqs. (4)–(9).

When light with energy greater than the bandgap of Fe^{3+} doped TiO_2 irradiates the material, photogenerated electrons and holes are formed:

$$TiO_2 + hv \rightarrow (TiO_2)e^- + h^+ \quad (4)$$

The Fe^{3+} ions in the TiO_2 matrix act as traps for both electrons and holes, forming Fe^{2+} and Fe^{4+} species. These oxidation states are less stable than Fe^{3+} due to its half-filled d^5 configuration:

$$Fe^{3+} + h^+ \rightarrow Fe^{4+} \quad (5)$$

$$Fe^{3+} + e^- \rightarrow Fe^{2+} \quad (6)$$

Fe^{2+} ions can transfer electrons to adsorbed O_2 molecules, forming reactive superoxide anions, while Fe^{4+} can react with hydroxyl groups to produce hydroxyl radicals:

$$Fe^{2+} + O_{2(ads)} \rightarrow Fe^{3+} + \cdot O_2^- \quad (7)$$

$$Fe^{4+} + OH^-_{(ads)} \rightarrow Fe^{3+} + \cdot OH_{(ads)} \quad (8)$$

Additionally, Fe^{2+} may reduce Ti^{4+} to Ti^{3+}, contributing to charge separation:

$$Fe^{2+} + Ti^{4+} \rightarrow Fe^{3+} + Ti^{3+} \quad (9)$$

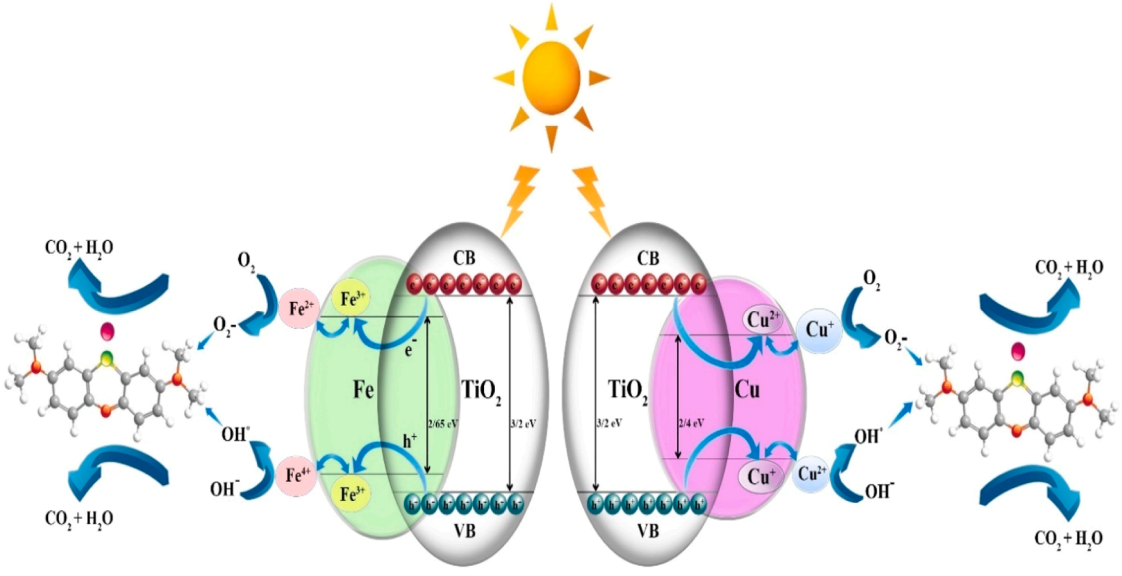

Fig. 8. A schematic representation of the possible photocatalytic mechanism in the degradation of MB dye for Cu–TiO_2 and Fe–TiO_2.

These reactions contribute to the generation of reactive species and suppress the recombination of photogenerated electron–hole pairs, leading to enhanced photocatalytic performance of Fe-doped TiO_2 under visible light.

The enhanced photocatalytic activity of Cu–TiO_2 nanostructures is explained by a multistep mechanism, analogous to that of Fe–TiO_2. Under visible light irradiation, electrons from the valence band of TiO_2 are excited and transferred to Cu^{2+} ions, resulting in the formation of Cu^{+} (Eq. (10)):

$$Cu^{2+} + e^{-} \rightarrow Cu^{+} \quad (10)$$

The redox potential of the Cu^{2+}/Cu^{+} couple is less negative than the conduction band edge of TiO_2, which favors charge carrier separation and suppresses recombination. The Cu^{+} species can further participate in redox reactions, reducing adsorbed oxygen molecules and facilitating the formation of superoxide anions via a multielectron transfer process (Eqs. (11) and (12)):

$$Cu^{+} + O_2 \rightarrow Cu^{2+} + e^{-} \quad (11)$$

$$e^{-} + O_{2(ads)} \rightarrow {}^{\cdot}O_2^{-} \quad (12)$$

Conversely, Cu^{+} can also be reoxidized to Cu^{2+} through hole trapping, further contributing to the redox cycle (Eq. (13)):

$$Cu^{+} + h^{+} \rightarrow Cu^{2+} \quad (13)$$

Cu^{2+} ions may then interact with adsorbed hydroxyl ions to generate hydroxyl radicals, enhancing the oxidation potential of the system (Eq. (14)):

$$Cu^{2+} + OH^{-}_{(ads)} \rightarrow Cu^{+} + {}^{\cdot}OH_{(ads)} \quad (14)$$

A series of subsequent redox reactions generates reactive oxygen species (ROS) and other oxidative radicals with high redox potential, ultimately degrading MB into CO_2 and H_2O. These processes are schematically illustrated in the following steps: (Eqs. (15)-(19)) [47]:

$$Ti^{3+} + O_{2(ads)} \rightarrow Ti^{3+} + {}^{\cdot}O_2^{-} \quad (15)$$

$$O_2^{-} + h^{+} \rightarrow 2O^{-} \quad (16)$$

$$O^{-} + h^{+} \rightarrow O^{\cdot} \quad (17)$$

$$O^{-} + H_2O \rightarrow {}^{\cdot}OH_{(ads)} + OH^{-}_{(ads)} \quad (18)$$

$$MB + {}^{\cdot}OH_{(ads)} \rightarrow H_2O + CO_2 \quad (19)$$

Thus, the Cu^{2+} and Fe^{3+} ions play a crucial role in redox reactions, facilitating the formation of ROS and improving charge separation. Furthermore, the incorporation of Fe and Cu significantly enhances photocatalytic activity by increasing light absorption through a reduction in the band gap. As a result, Cu^{2+} and Fe^{3+} ions effectively improve the photocatalytic efficiency of TiO_2 nanoparticles, particularly for the degradation of MB pollutant.

3.6. Antimicrobial activity

The bacterial inactivation percentages for 0.8Cu–TiO_2, 3Fe–TiO_2, and pure TiO_2, as the most promising doped samples and the undoped one were calculated using the following equation [48]:

$$r = \frac{N_0 - N}{N_0} \cdot 100 \quad (20)$$

where r represents the bacterial inactivation percentage, N_0 (CFU/mL) is the initial bacterial concentration, and N is the viable bacterial concentration after visible light irradiation. Fig. 9 shows the percentage reduction in *Escherichia coli* colonies for pure TiO_2, 0.8Cu–TiO_2, and 3Fe–TiO_2 following irradiation for 1, 2, and 3 h. Corresponding images

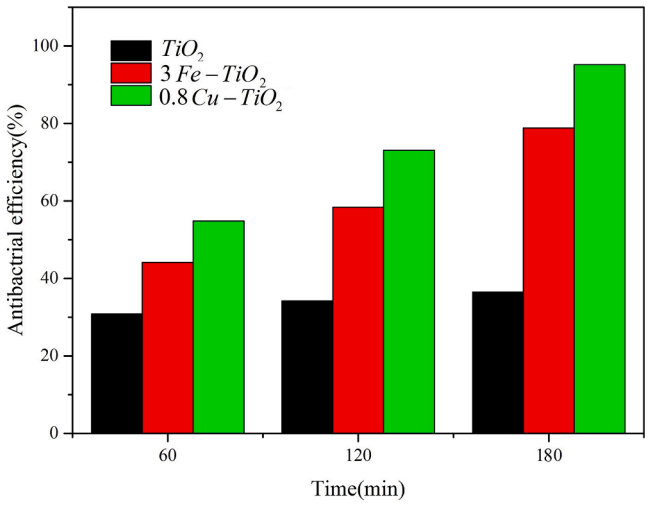

Fig. 9. Relative antibacterial efficiency for TiO_2, 3Fe–TiO_2 and 0.8Cu–TiO_2 samples.

of bacterial growth after treatment are provided in Fig. 10.

Among all samples, 0.8Cu–TiO_2 exhibited the highest antibacterial performance, achieving inactivation efficiencies of 58 %, 78 %, and 95 % after 1, 2, and 3 h of visible light exposure, respectively. In contrast, 3Fe–TiO_2 reached 42 %, 59 %, and 79 % efficiency at the same time intervals, while pure TiO_2 achieved only 34 % inactivation by the end of the 3-hour period. These results confirm that 0.8Cu–TiO_2 is the most effective antimicrobial agent among tested materials.

Moreover, both 0.8Cu–TiO_2 and 3Fe–TiO_2 demonstrated significantly enhanced antibacterial activity over the time compared to undoped TiO_2. This improvement is attributed to the incorporation of Cu^{2+} and Fe^{3+} ions into the TiO_2 lattice, which is believed to introduce shallow trapping sites at donor and acceptor energy levels, thereby facilitating enhanced reactive oxygen species (ROS) generation under visible light.

The superior antibacterial performance of 0.8Cu–TiO_2 can be attributed to multiple synergistic factors. Firstly, 0.8Cu–TiO_2 exhibits greater sensitivity to visible light and a lower band gap compared to both Fe-doped and undoped TiO_2, thereby enhancing its photocatalytic and antibacterial efficacy (Section 3.3) [49]. As discussed previously, the reduced band gap is critical for promoting the generation of reactive oxygen species (ROS), such as hydroxyl ($^{\bullet}OH$) and superoxide ($^{\bullet}O_2^{-}$) radicals, which are known to effectively disrupt bacterial membranes and cellular components [50], together with the lower recombination rate.

In addition, 0.8Cu–TiO_2 bears a smaller crystallite size than both 3Fe–TiO_2 and pure TiO_2 (Section 3.1 and 3.2), resulting in a higher specific surface area (SSA). This increased surface area allows for more efficient contact between the photocatalyst and bacterial cells, thereby enhancing the interaction with ROS and improving antibacterial outcomes [51].

Overall, the enhanced antibacterial activity of 0.8Cu–TiO_2 against *Escherichia coli*, as compared to Fe–TiO_2 and undoped TiO_2, can be attributed to a combination of the intrinsic antimicrobial properties of copper, the reduced band gap facilitating ROS generation under visible light, and the increased surface area associated with smaller crystallite size [10].

The most widely accepted mechanism of ROS attack on Escherichia coli is depicted in Fig. 11. The photogenerated h^{+} reacts with water molecules to produce hydroxyl radicals ($^{\bullet}OH$), while e^{-} reacts with oxygen molecules to form superoxide radicals ($^{\bullet}O_2^{-}$). These reactive species damage the bacterial structure upon exposure [52,53].

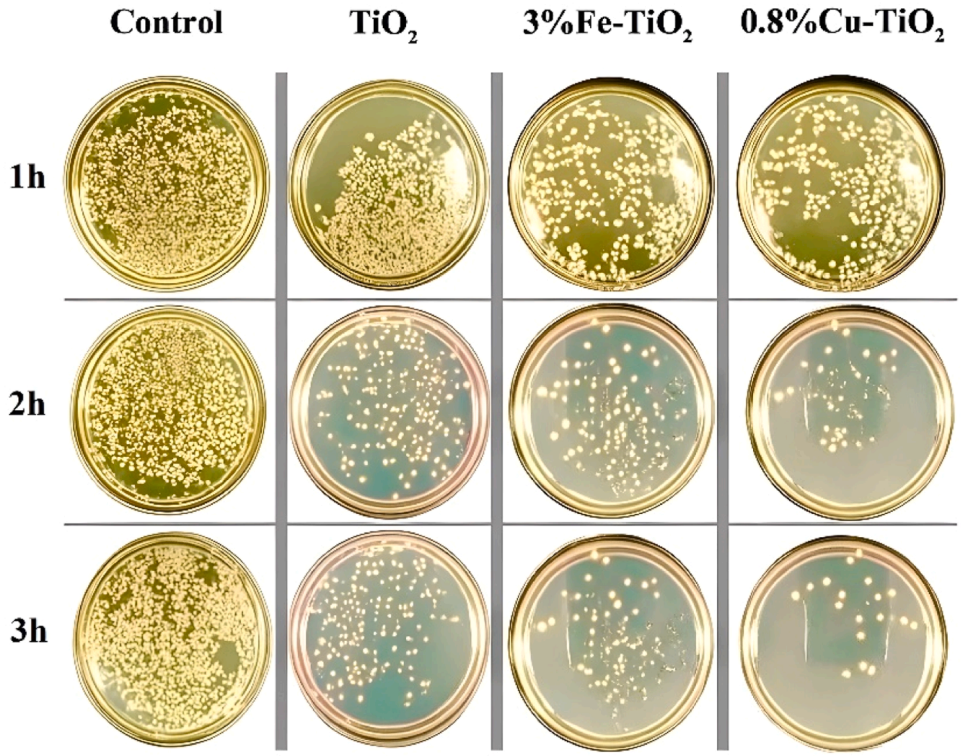

Fig. 10. Images of control (glass), TiO_2, 3Fe–TiO_2 and 0.8Cu–TiO_2 in contact with *Escherichia coli* under visible light irradiation for 1, 2 and 3 h.

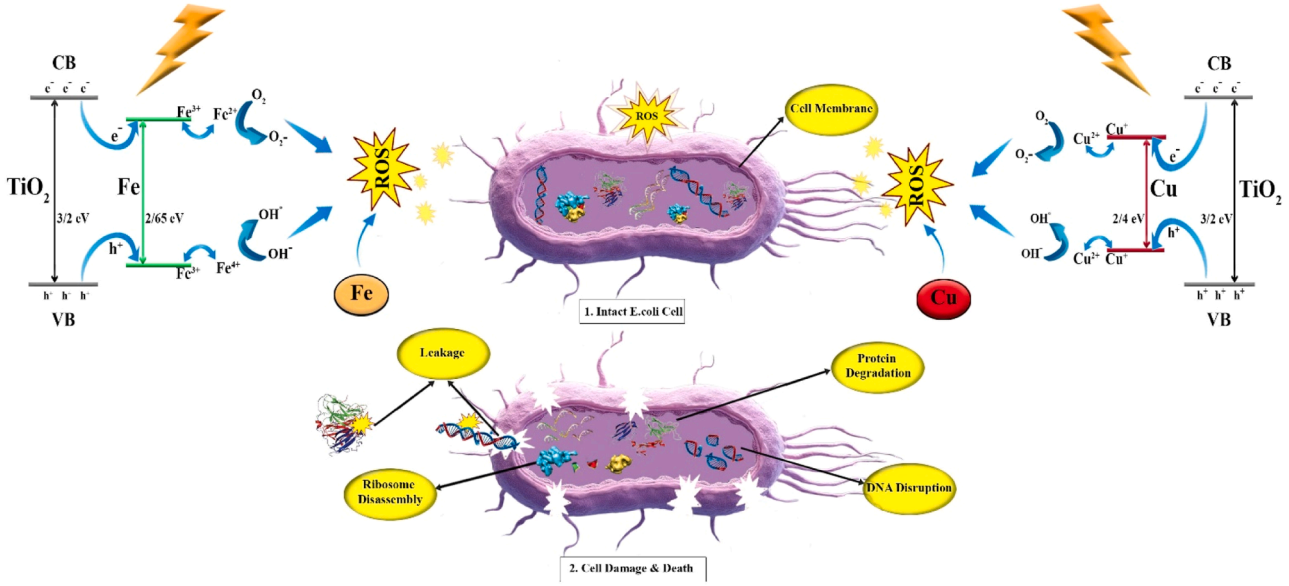

Fig. 11. Mechanisms of the Fe–TiO_2 and Cu–TiO_2 against *Escherichia coli*. On the left and right side of the Figure, the activation of the photocatalytic semiconductor of Fe–TiO_2 and Cu–TiO_2 by visible light is illustrated.

3.7. Water contact angle measurements

Finally, the hydrophilic behavior of TiO_2 and metal-doped TiO_2 samples was evaluated through Water Contact Angle (WCA) measurements. WCA results of samples irradiated with visible light are summarized in Fig. 12. It can be noted that the addition of Cu and Fe increases the hydrophilicity of TiO_2-based coating. The WCA value of pure TiO_2 thin film was 68°, while Cu and Fe doped thin films showed less WCA values, therefore more hydrophilic character. Among the Cu doped samples, 0.8Cu–TiO_2 exhibited a super-hydrophilic (WCA < 10°), showing the lowest contact angle of 9.8°. However, as the Cu doping level increased, the WCA rose significantly, reaching 17°, 36° and 40° for 1.5Cu–TiO_2, 2.2Cu–TiO_2 and 3Cu–TiO_2, respectively. In general, elemental copper exhibits super-hydrophilicity, whereas the copper oxide (CuO) shows less hydrophilicity [54]. Therefore, it can be concluded that the higher hydrophobic character of 1.5Cu–TiO_2, 2.2Cu–TiO_2 and 3Cu–TiO_2 samples may be related to the higher proportion of CuO clusters in these samples, in line with XRD and EDX findings [55,56].

Regarding Fe doped TiO_2 thin films, they demonstrated more

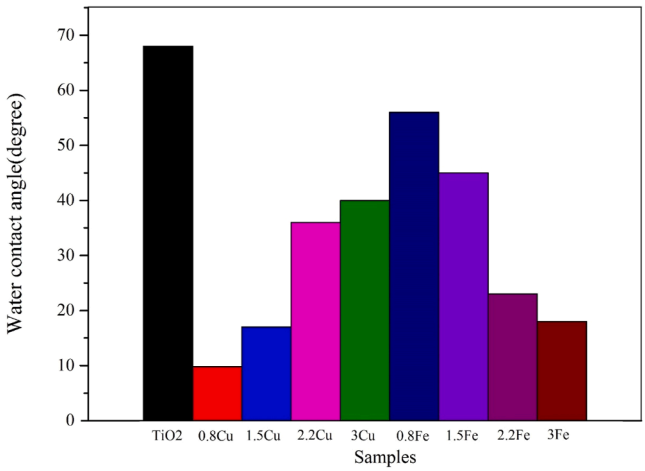

Fig.12. Contact angle measurement of pure TiO_2, Cu and Fe doped TiO_2.

hydrophilic character than pure TiO_2. It was revealed that the addition of Fe caused more hydrophilicity, from 56° for 0.8Fe–TiO_2 to 45°, 23° and 18.8° for 1.5Fe–TiO_2, 2.2Fe–TiO_2 and 3Fe–TiO_2, respectively. The improved hydrophilicity of doped coating can be attributed to their higher number of oxygen vacancies compared to those of TiO_2. The numerous oxygen vacancies are associated with a greater content of hydroxyl groups, which makes the surface of the doped coating more hydrophilic. The formation of more hydroxyl groups in more hydrophilic coatings can be beneficial for trapping the generated holes and preventing the recombination of electron and holes. This improvement can enhance the photocatalytic behavior of the coatings [57,58]. A typical shape of 5μl water droplet over pure TiO_2, 3Fe- and 0.8Cu-doped TiO_2 thin films irradiated on visible light are illustrated in Fig. 13. It can be noted that both doped films reveal more hydrophilic character as the WCA of undoped TiO_2 decreased from 68° to 18.8° (3Fe) and 9.8° (0.8Cu).

4. Conclusions

In this study, TiO_2 nanoparticles doped with varying weight percentages of Cu and Fe (x = 0.8, 1.5, 2.2, and 3.0) were successfully synthesized via the sol–gel method using dip-coating procedure followed by calcination at 500 °C. The outcomes of this study allow to draw the following conclusions:

- Structural and morphological characterization showed that all samples retained the anatase crystalline phase. Crystallite sizes ranged from ~12–27 nm for Cu–TiO_2 and 18–30 nm for Fe–TiO_2, compared to 37 nm for undoped TiO_2. FE–SEM revealed that particle sizes were also significantly reduced upon doping, with pure TiO_2 exhibiting particles of ~120 nm, while 0.8Cu–TiO_2 and 3Fe–TiO_2 had sizes of 28 nm and 75 nm, respectively. These reductions in size led to higher specific surface areas and enhanced photocatalytic performance.
- Optical characterization indicated a band gap narrowing from ~3.20 eV (pure TiO_2) to ~2.40 eV (0.8Cu–TiO_2) and ~2.65 eV (3Fe–TiO_2), as shown in the Tauc plots. Doping improved visible-light absorption and promoted charge separation. However, excessive Cu loading caused agglomeration and structural disorder, leading to band gap widening and diminished photocatalytic performance. In contrast, Fe doping maintained dispersion even at higher concentrations, allowing continuous band gap reduction and enhanced activity. PL spectroscopy indicated a reduced electron-hole recombination for the doped photocatalysts, especially for 0.8Cu–TiO_2 and 3Fe–TiO_2.
- Photocatalytic activity, assessed via MB removal, demonstrated superior performance for 0.8Cu–TiO_2 (~80 %), followed by 3Fe–TiO_2 (~65 %) and pure TiO_2 (~15 %). Similarly, antibacterial tests showed *Escherichia coli* inactivation efficiencies of 95 % for 0.8Cu–TiO_2, 79 % for 3Fe–TiO_2, and 34 % for undoped TiO_2 after 3 h under visible light. Moreover, the WCA results of pure TiO_2 and doped samples are consistent with their antimicrobial activities, as the 0.8Cu-TiO_2 thin film exhibits super-hydrophilicity compared to the other samples. These findings confirm the crucial role of dopant concentration in enhancing photocatalytic and antibacterial performance.

In summary, this study highlights the importance of selecting appropriate dopants and their optimal concentrations to design highly efficient TiO_2-based photocatalysts. The 0.8Cu–TiO_2 photocatalyst can be considered as a promising candidate for water treatment, self-cleaning and antimicrobial applications under visible light irradiation.

Associated content

Notes

The authors declare that they have no conflict of interest.

Funding

This research did not receive any specific grant from funding agencies in the public, commercial, or not-for-profit sectors.

CRediT authorship contribution statement

Ehsan Mehmandoustesfahani: Writing – original draft, Validation, Methodology, Investigation, Formal analysis, Data curation. **Fatemeh Hakimi:** Writing – original draft, Validation, Methodology, Investigation, Formal analysis. **Jorge Rodríguez-Chueca:** Writing – review & editing, Supervision. **José Antonio Díaz–López:** Writing – review & editing, Validation, Formal analysis, Conceptualization. **Antonio Nieto–Márquez:** Writing – review & editing, Validation, Supervision, Project administration, Formal analysis, Conceptualization.

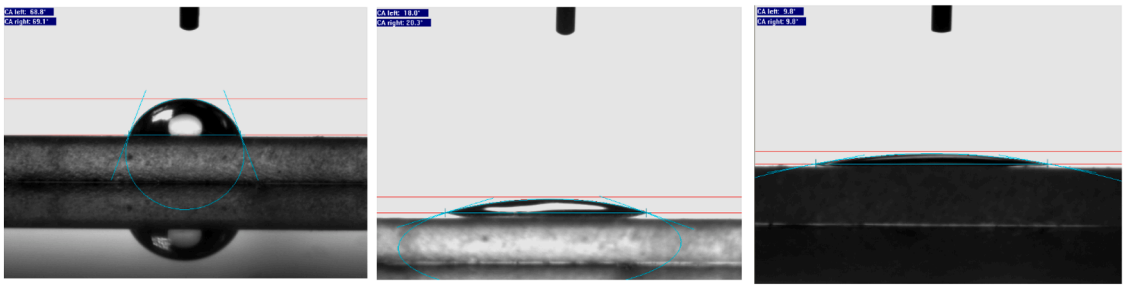

Fig.13. Water contact angle images of (a) pure TiO_2 (b) 3Fe–TiO_2 (c) 0.8Cu–TiO_2.

Declaration of competing interest

The authors declare that they have no known competing financial interests or personal relationships that could have appeared to influence the work reported in this paper.

References

[1] B. Pant, et al., Carbon nanofibers decorated with binary semiconductor (TiO_2/ZnO) nanocomposites for the effective removal of organic pollutants and enhancement of antibacterial activities, Ceram. Int. 39 (2013) 7807–7816, https://doi.org/10.1016/j.ceramint.2013.02.041.

[2] J. Liu, et al., Efficient photocatalytic degradation of imidazolium ionic liquids in an N-ZnO/simulated sunlight irradiation system and its mechanism, Chem. Eng. J. 401 (2024) 126296, https://doi.org/10.1016/j.cej.2024.154317.

[3] Q. Sun, N. Wang, J. Yu, J.C. Yu, A hollow porous CdS photocatalyst, Adv. Mater. 30 (2018) 180436, https://doi.org/10.1002/adma.201804368.

[4] M. Mohadesi, M. Sanavi Fard, A. Shokri, The application of modified nano-TiO_2 photocatalyst for wastewater treatment, Int. J. Environ. Anal. Chem. 104 (2024) 204–220, https://doi.org/10.1080/03067319.2022.2064751.

[5] M. Ikram, et al., Dye degradation performance, bactericidal behavior, and molecular docking analysis of Cu-doped TiO_2 nanoparticles, RSC Adv 10 (2020) 28551–28564, https://doi.org/10.1039/D0RA04851H.

[6] S. Reghunath, D. Pinheiro, A review of hierarchical nanostructures of TiO_2: advances and applications, Appl. Surf. Sci. Adv. 5 (2021) 100063, https://doi.org/10.1016/j.apsadv.2021.100063.

[7] C. Karunakaran, G. Abiramasundari, P. Gomathisankar, G. Manikandan, V. Anandi, Cu-doped TiO_2 nanoparticles for photocatalytic disinfection of bacteria under visible light, J. Colloid Interface Sci. 350 (2010) 269–276, https://doi.org/10.1016/j.jcis.2010.08.012.

[8] S.M.H. Al-Jawad, A.A. Taha, M.M. Salim, Synthesis and characterization of pure and Fe-doped TiO_2 thin films for antimicrobial activity, Optik (Stuttg) 142 (2017) 42–53, https://doi.org/10.1016/j.ijleo.2017.05.048.

[9] E. Montakhab, F. Rashchi, S. Sheibani, Enhanced photocatalytic activity of TiO_2 nanotubes decorated with Ag nanoparticles by simultaneous electrochemical deposition and reduction processes, Appl. Surf. Sci. 615 (2023) 156332, https://doi.org/10.1016/j.apsusc.2023.156332.

[10] Y. Mingmongkol, et al., Enhanced photocatalytic and photokilling activities of Cu-doped TiO_2 nanoparticles, Nanomaterials 12 (2022) 1198, https://doi.org/10.3390/nano12071198.

[11] S. Mathew, et al., Cu-doped TiO_2: visible light assisted photocatalytic antimicrobial activity, Appl. Sci. 8 (2018) 2067, https://doi.org/10.3390/app8112067.

[12] S. Naghibi, S. Vahed, O. Torabi, Evaluation of photocatalytic activity of Fe-doped TiO_2 thin film prepared by sol-gel hot dip-coating, J. Adv. Mater. Process. 2 (2014) 55.

[13] N. Negishi, T. Iyoda, K. Hashimoto, A. Fujishima, Preparation of transparent TiO_2 thin film photocatalyst and its photocatalytic activity, Chem. Lett. 24 (1995) 841–842, https://doi.org/10.1246/cl.1995.841.

[14] H.-J. Nam, T. Amemiya, M. Murabayashi, K. Itoh, Photocatalytic activity of sol-gel TiO_2 thin films on various kinds of glass substrates: the effects of Na^+ and primary particle size, J. Phys. Chem. B 108 (2004) 8254–8259, https://doi.org/10.1021/jp037170t.

[15] M.C. Hidalgo, S. Sakthivel, D. Bahnemann, Highly photoactive and stable TiO_2 coatings on sintered glass, Appl. Catal. A Gen. 277 (2004) 183–189, https://doi.org/10.1016/j.apcata.2004.09.011.

[16] B. Pava-Gómez, X. Vargas-Ramírez, C. Díaz-Uribe, H. Romero, F. Duran, Evaluation of copper-doped TiO_2 film supported on glass and LDPE with the design of a pilot-scale solar photoreactor, Sol. Energy 220 (2021) 695–705, https://doi.org/10.1016/j.solener.2021.03.071.

[17] N. Mokhtari, A.R. Solaimany Nazar, M. Farhadian, P. Eskandari, B. Jeon, Silver deposition on titanium oxide thin glass films for efficient visible light-induced photocatalytic removal of diphenhydramine and venlafaxine, Int. J. Environ. Sci. Technol. 19 (2022) 12465–12476, https://doi.org/10.1007/s13762-022-04486-0.

[18] M.B. Marami, M. Farahmandjou, B. Khoshnevisan, Sol-gel synthesis of Fe-doped TiO_2 nanocrystals, J. Electron. Mater. 47 (2018) 3741–3748, https://doi.org/10.1007/s11664-018-6234-5.

[19] T. Aguilar, et al., A route for the synthesis of Cu-doped TiO_2 nanoparticles with a very low band gap, Chem. Phys. Lett. 571 (2013) 49–53, https://doi.org/10.1016/j.cplett.2013.04.007.

[20] T.S. Nirmala, N. Iyandurai, S. Yuvaraj, M. Sundararajan, Effect of Cu^{2+} ions on structural, morphological, optical and magnetic behaviors of $ZnAl_2O_4$ spinel, Mater. Res. Express 7 (2020) 046104, https://doi.org/10.1088/2053-1591/ab7a7a.

[21] T. Tian, J. Zhang, L. Tian, S. Ge, Z. Zhai, Photocatalytic degradation of gaseous benzene using Cu/Fe-doped TiO_2 nanocatalysts under visible light, Molecules 29 (2023) 144, https://doi.org/10.3390/molecules29010144.

[22] M. Dhonde, K.S. Dhonde, V.V.S. Murty, Novel sol-gel synthesis of Al/N co-doped TiO_2 nanoparticles and their structural, optical, and photocatalytic properties, J. Mater. Sci. Mater. Electron. 29 (2018) 18465–18475, https://doi.org/10.1007/s10854-018-9962-7.

[23] V. Rajendran, R. Gandhimathi, M. Sankareswari, K. Neyvasagam, Influence of Cu concentration on the structural, morphological, optical, and catalytic properties of TiO_2 thin films, Indian J. Pure Appl. Phys. 57 (2019) 475–482.

[24] T. Raguram, K.S. Rajni, Synthesis and analyzing the structural, optical, morphological, photocatalytic, and magnetic properties of TiO_2 and doped (Ni and Cu) TiO_2 nanoparticles by sol-gel technique, Appl. Phys. A 125 (2019) 1–11, https://doi.org/10.1007/s00339-019-2581-1.

[25] T. Suprabha, H.G. Roy, J. Thomas, K.Praveen Kumar, S. Mathew, Microwave-assisted synthesis of titania nanocubes, nanospheres and nanorods for photocatalytic dye degradation, Nanoscale Res. Lett. 4 (2009) 144–152, https://doi.org/10.1007/s11671-008-9214-5.

[26] A. Seifi, D. Salari, A. Khataee, B. Çoşut, L. Arslan, A. Niaei, Enhanced photocatalytic activity of highly transparent superhydrophilic doped TiO_2 thin films for improving the self-cleaning property of solar panel covers, Ceram. Int. 49 (2023) 1678–1689, https://doi.org/10.1016/j.ceramint.2022.09.130.

[27] B. Houng, C.C. Liu, M.T. Hung, Structural, electrical and optical properties of molybdenum-doped TiO2 thin films, Ceram. Int. 39 (2013) 3669–3676, https://doi.org/10.1016/j.ceramint.2012.10.197.

[28] M.N. Islam, J. Podder, The role of aluminum, cobalt co-doping on the band gap tuning of TiO_2 thin film deposited by spray pyrolysis, Mater. Sci. Semicond. Process. 121 (2019) 105419, https://doi.org/10.1016/j.mssp.2020.105419.

[29] S. Munir, S.M. Shah, H. Hussain, Effect of carrier concentration on the optical band gap of TiO_2 nanoparticles, Mater. Des. 92 (2016) 64–72, https://doi.org/10.1016/j.matdes.2015.12.022.

[30] D.C. Agarwal, et al., Enhanced room temperature ferromagnetism and green photoluminescence in Cu-doped ZnO thin film synthesized by neutral beam sputtering, Sci. Rep. 9 (2019) 6675, https://doi.org/10.1038/s41598-019-43184-9.

[31] M. Rizwan, et al., Putting DFT to trial: for the exploration to correlate structural, electronic, and optical properties of M-doped (M = Group I, II, III, XII, XVI) lead-free high piezoelectric c-$BiAlO_3$, Mater. Sci. Eng. B 264 (2021) 114959, https://doi.org/10.1016/j.mseb.2020.114959.

[32] V.R. Akshay, et al., Defect mediated mechanism in undoped, Cu and Zn-doped TiO_2 nanocrystals for tailoring the band gap and magnetic properties, RSC Adv 8 (2018) 41994–42008, https://doi.org/10.1039/C8RA07287F.

[33] F. Qin, et al., Enhanced photocatalytic activity of g-C_3N_4/Bi_2WO_6 heterojunction via Z-scheme charge-transfer mechanism, J. Mol. Struct. 1301 (2024) 139023, https://doi.org/10.1016/j.molstruc.2024.139023.

[34] F. Qin, et al., Enhanced charge transfer and photocatalytic activity of BiOBr/Bi_2WO_6 p-n heterojunctions, J. Mol. Struct. 1300 (2024) 137719, https://doi.org/10.1016/j.molstruc.2024.137719.

[35] H. Rasoulnezhad, G. Hosseinzadeh, N. Ghasemian, R. Hosseinzadeh, A. Homayoun Keihan, Transparent nanostructured Fe-doped TiO_2 thin films prepared by ultrasonic assisted spray pyrolysis technique, Mater. Res. Express 5 (2018) 056401, https://doi.org/10.1088/2053-1591/aabe5e.

[36] S. Ahadi, N.S. Moalej, S. Sheibani, Characteristics and photocatalytic behavior of Fe and Cu doped TiO_2 prepared by combined sol–gel and mechanical alloying, Solid State Sci. 96 (2019) 105975, https://doi.org/10.1016/j.solidstatesciences.2019.105975.

[37] A.M. Alotaibi, B.A.D. Williamson, S. Sathasivam, A. Kafizas, M. Alqahtani, C. Sotelo-Vazquez, J. Buckeridge, S.P. Nair, D.O. Scanlon, I.P. Parkin, J. Wu, Enhanced photocatalytic and antibacterial ability of Cu-doped anatase TiO_2 thin films: theory and experiment, ACS Appl. Mater. Interfaces 12 (2020) 15348–15358, https://doi.org/10.1021/acsami.9b22056.

[38] A. El Mragui, I. Aadnan, O. Zegaoui, J.C.G. Esteves da Silva, Physico-chemical characterization and photocatalytic activity assessment under UV-A and visible-light irradiation of iron-doped TiO_2 nanoparticles, Arab, J. Chem. 16 (2023) 105331, https://doi.org/10.1016/j.arabjc.2023.105331.

[39] D. Li, Z. Liang, W. Zhang, S. Dai, C. Zhang, Preparation and photocatalytic performance of TiO_2-RGO-CuO/Fe_2O_3 ternary composite photocatalyst by solvothermal method, Mater. Res. Express 8 (2021) 015025, https://doi.org/10.1088/2053-1591/abdc3b.

[40] H. Zhang, M. Wang, F. Xu, Generating oxygen vacancies in Cu^{2+}-doped TiO_2 hollow spheres for enhanced photocatalytic and antimicrobial activity, Micro Nano Lett. 15 (2020) 535–539, https://doi.org/10.1049/mnl.2019.0781.

[41] X. Yang, W. Shu, H. Sun, X. Wang, J. Lian, Preparation and photocatalytic performance of Cu-doped TiO_2 nanoparticles, Trans. Nonferrous Met. Soc. China 25 (2015) 504–509, https://doi.org/10.1016/S1003-6326(15)63631-7.

[42] X. Xu, Y. Wang, R. Wang, J. Pan, J. Hu, H. Zeng, Creating carbon-oxygen bonds over TiO_2 nanofibers for synergistic benefits of visible-light response and charge separation toward photocatalysis, Adv. Mater. Interfaces 4 (2017) 1600795, https://doi.org/10.1002/admi.201600795.

[43] Y. Yao, C. Huang, Y. Yang, M. Li, B. Ren, Electrochemical removal of thiamethoxam using three-dimensional porous PbO_2–CeO_2 composite electrode: electrode characterization, operational parameters optimization and degradation pathways, Chem. Eng. J. 350 (2018) 960–970, https://doi.org/10.1016/j.cej.2018.06.036.

[44] C. Xu, G.P. Rangaiah, X.S. Zhao, Photocatalytic degradation of methylene blue by titanium dioxide: experimental and modeling study, Ind. Eng. Chem. Res. 53 (2014) 14641–14649, https://doi.org/10.1021/ie502367x.

[45] C. Thambiliyagodage, S. Mirihana, Photocatalytic activity of Fe and Cu co-doped TiO_2 nanoparticles under visible light, J. Sol-Gel Sci. Technol. 99 (2021) 109–121, https://doi.org/10.1007/s10971-021-05556-4.

[46] S. Saroj, L. Singh, R. Ranjan, S.V. Singh, Enhancement of photocatalytic activity and regeneration of Fe-doped TiO_2 ($Ti_{1-x}Fe_xO_2$) nanocrystalline particles synthesized using inexpensive TiO_2 precursor, Res. Chem. Intermed. 45 (2019) 1883–1900, https://doi.org/10.1007/s11164-018-3708-2.

[47] S. Sood, A. Umar, S.K. Mehta, S.K. Kansal, Highly effective Fe-doped TiO_2 nanoparticles photocatalysts for visible-light driven photocatalytic degradation of

toxic organic compounds, J. Colloid Interface Sci. 450 (2015) 213–223, https://doi.org/10.1016/j.jcis.2015.03.018.
[48] U. Werapun, J. Pechwang, Synthesis and antimicrobial activity of Fe:TiO_2 particles, J. Nano Res. 56 (2019) 28–38, https://doi.org/10.4028/www.scientific.net/JNanoR.56.28.
[49] K. Suzuki, et al., Antibacterial properties of Cu-doped TiO_2 prepared by chemical and heat treatment of Ti metal, J. Asian Ceram. Soc. 9 (2021) 1448–1456, https://doi.org/10.1080/21870764.2021.1979287.
[50] Z.N. Kayani, I. Wahid, Z. Saddiqe, S. Riaz, S. Waseem, S. Naseem, Tailoring of optical, biological and magnetic properties of nanocrystalline Fe-doped TiO_2 thin films, Mater. Res. Express 6 (2020) 1250H, https://doi.org/10.1088/2053-1591/ab6b5a.
[51] A. Zielińska-Jurek, Z. Wei, I. Wysocka, P. Szweda, E. Kowalska, The effect of nanoparticle size on photocatalytic and antimicrobial properties of Ag-Pt/TiO_2 photocatalysts, Appl. Surf. Sci. 353 (2015) 317–325, https://doi.org/10.1016/j.apsusc.2015.06.065.
[52] C. Regmi, B. Joshi, S.K. Ray, G. Gyawali, R.P. Pandey, Understanding mechanism of photocatalytic microbial decontamination of environmental wastewater, Front. Chem. 6 (2018) 33, https://doi.org/10.3389/fchem.2018.00033.
[53] J. Li, et al., Antibacterial activity of large-area monolayer graphene film manipulated by charge transfer, Sci. Rep. 4 (2014) 4359, https://doi.org/10.1038/srep04359.
[54] S. Wang, K.K. Meng, L. Zhao, Q. Jiang, J.S. Lian, Superhydrophilic Cu-doped TiO_2 thin film for solar-driven photocatalysis, Ceram. Int. 40 (2014) 5107–5110, https://doi.org/10.1016/j.ceramint.2013.09.028.
[55] A. Eshaghi, A. Eshaghi, Preparation and hydrophilicity of TiO_2 sol–gel derived nanocomposite films modified with copper loaded TiO_2 nanoparticles, Mater. Res. Bull. 46 (2011) 2342–2345, https://doi.org/10.1016/j.materresbull.2011.08.035.
[56] Y. Xu, J.A. Li, L.F. Yao, L.H. Li, P. Yang, N. Huang, Preparation and characterization of Cu-doped TiO_2 thin films and effects on platelet adhesion, Surf. Coat. Technol. 261 (2015) 436–441, https://doi.org/10.1016/j.surfcoat.2014.09.031.
[57] J.-J. Park, D.-Y. Kim, S.S. Latthe, J.-G. Lee, M.T. Swihart, S.S. Yoon, Thermally induced superhydrophilicity in TiO_2 films prepared by supersonic aerosol deposition, ACS Appl. Mater. Interfaces 5 (2013) 6155–6160, https://doi.org/10.1021/am401083y.
[58] G. Garlisi, G. Palmisano, Radiation-free superhydrophilic and antifogging properties of e-beam evaporated TiO_2 films on glass, Appl. Surf. Sci. 420 (2017) 83–93, https://doi.org/10.1016/j.apsusc.2017.05.077.